Supplementary Materials

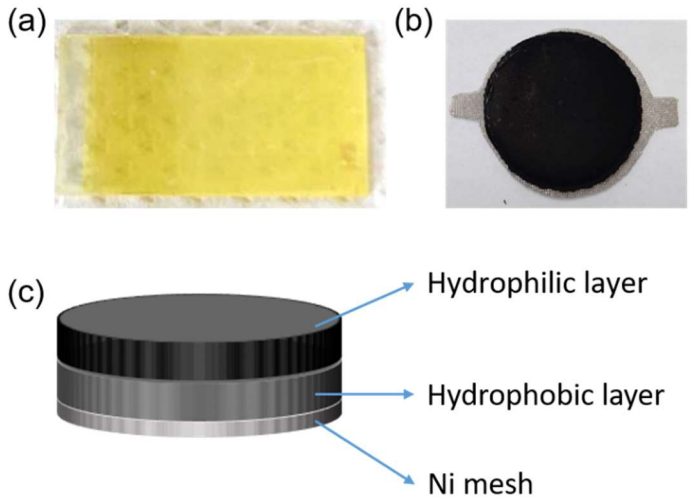

Figure S1. Photos of (**a**) WO_3/BVO photoanode and (**b**) SnPc-GDE. (**c**) Schematic diagram of the structure of GDE. The bottom layer is the Ni network, the middle is the hydrophobic layer, and the top layer is the hydrophilic layer.

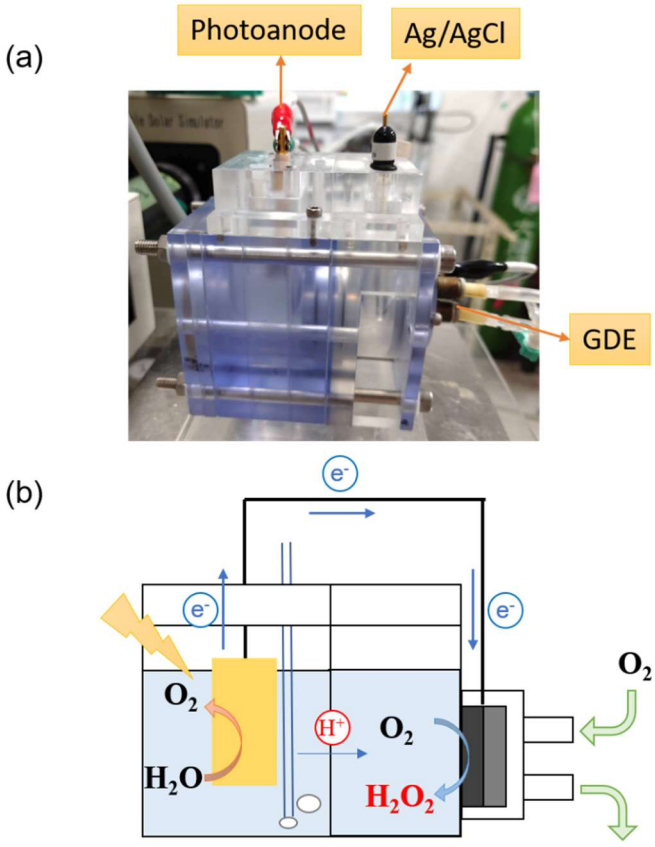

Figure S2. (**a**) Photo of the PEC system. (**b**) Schematic diagram of the PEC system.

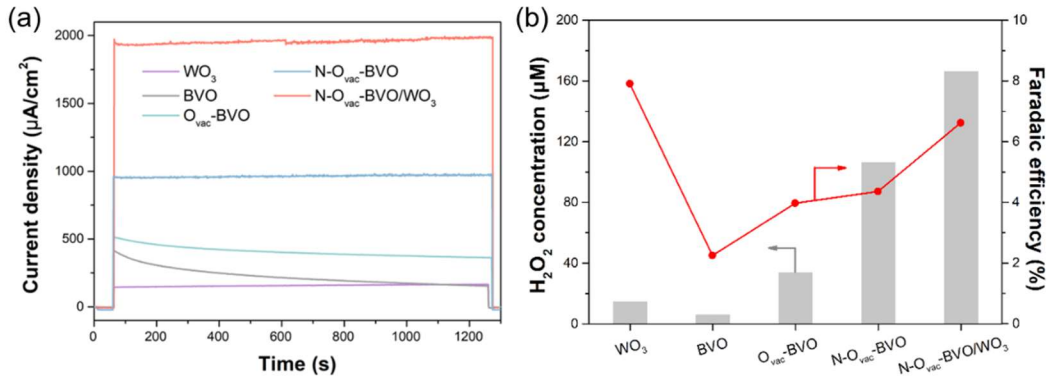

Figure S3. (**a**) CA curves of WO_3, BVO, O_{vac}-BVO, N-O_{vac}-BVO, and N-O_{vac}-BVO/WO_3 photoanodes under the potential of 1.5 V_{RHE}. (**b**) Amount of H_2O_2 generated by WO_3, BVO, O_{vac}-BVO, N-O_{vac}-BVO, and N-O_{vac}-BVO/WO_3 photoanodes in a CO_2-bubbling $KHCO_3$ electrolyte (1 M, pH = 7.6) under the potential of 1.5 V_{RHE} with visible light irradiation (420–800 nm, 100 mW/cm^2) and Pt electrode as a counter electrode.

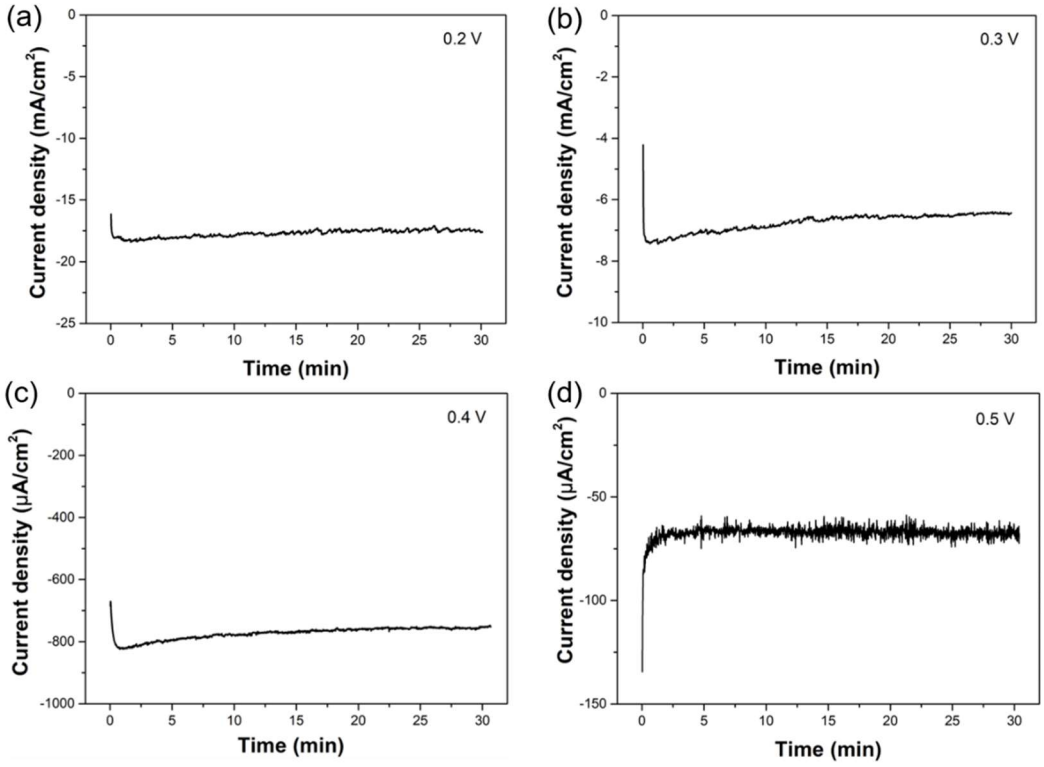

Figure S4. Time courses of the photocurrents of SnPc-GDE in an air-bubbling phosphate buffer electrolyte (0.5 M, pH = 6.5) under different potential conditions with visible light irradiation (420–800 nm, 100 mW/cm^2).

Table S1. Comparison of different photocathodes for H_2O_2 producing with current study

Photocathode	Light source	Added bias	Rate of producing H_2O_2	Faraday efficiency	Ref.
SnPc-GDE	420-800 nm 100 mW/cm^{-2}	0.2 V vs. RHE	16288.3 μM/h	98%	This work
		0.44 V vs. RHE	952.5 μM/h	48%	
Au-In_2S_3/Cu_3BiS_3	420-800 nm 100 mW/cm^{-2}	0.40 V vs. RHE	161.7 μM/h	71%	[1]
GDE/Ag/Ag-BiW_2O_8 /Bi_2WO_6	AM 1.5G	-0.1 V vs. RHE	193 μM/h	-	[2]
BH_4 dyes sensitized NiO	λ>400 nm 100 mW/cm^{-2}	0.42 V vs. RHE	53.8 μM/h	60%	[3]
$BiFeO_3$	AM 1.5G	0.6 V vs. RHE	45.6 μM/h	19%	[4]
Eumelanin	White LED 255 mW/cm^{-2}	0.26 V vs. RHE	29.2 μM/h	90%	[5]
PN/Au/PTCDI	Tungsten halogen lamp 100 mW/cm^{-2}	0.32 V vs. RHE	-	60-80%	[6]
$LaNiO_3$/$BiFeO_3$	AM 1.5G	0.6 V vs. RHE	91.7 μM/h	39%	[7]
Gd-doped CuBi2O4/CuO	AM 1.5G sunlight	0.65 V vs. RHE	2.6 mM/h	-	[8]

[1] C. Chen, M. Yasugi, L. Yu, Z. Teng, T. Ohno, Visible light-driven H2O2 synthesis by a Cu3BiS3 photocathode via a photoelectrochemical indirect two-electron oxygen reduction reaction. Applied Catalysis B: Environmental 2022, 307, 121152. https://doi:10.1016/j.apcatb.2022.121152.

[2] J.F. de Medeiros, M. Tayar Galante, R. Bertazzoli, C.G.P. dos Santos, C. Longo, Solar-driven photoreactor for water remediation based on n-type TiO2 and p-type Ag/AgBiW2O8/Bi2WO6 light-responsive air-fed gas diffusion electrodes. ACS ES&T Water, 2022, 2, 982-993. https://doi.org/10.1021/acsestwater.1c00471.

[3] J. Sun, Y. Yu, A. E. Curtze, X. Liang, Y. Wu, Dye-sensitized photocathodes for oxygen reduction: efficient H2O2 production and aprotic redox reactions, Chem. Sci., 2019, 10, 5519-5527. https://doi.org/10.1039/C9SC01626K.

[4] B. Tan, A.M. Reyes, E. Menéndez-Proupin, S.E. Reyes-Lillo, Y. Li, Z. Zhang, Full-space potential gradient driven charge migration inside BiFeO3 photocathode, ACS Energy Letters, 2022, 7, 3492-3499. https://doi.org/10.1021/acsenergylett.2c01750.

[5] L. Migliaccio, M. Gryszel, V. Đerek, A. Pezzella, E. D. Głowacki, Aqueous photo(electro)catalysis with eumelanin thin films, Mater. Horiz., 2018, 5, 984-990. https://doi.org/10.1039/C8MH00715B.

[6] M. Gryszel, A. Markov, M. Vagin, E. D. Głowacki, Organic heterojunction photocathodes for optimized photoelectrochemical hydrogen peroxide production, J. Mater. Chem. A, 2018, 6, 24709-24716. https://doi.org/10.1039/C8TA08151D.

[7] B. Tan, M. Sun, B. Liu, X. Jiang, Q. Feng, E. Xie, P. Xi, Z. Zhang, Boosting photocarrier collection in semiconductors by synergizing photothermoelectric and photoelectric. Nano Energy, 2023, 107, 108138. https://doi.org/10.1016/j.nanoen.2022.108138.

[8] Z. Li, Q. Xu, F. Gou, B. He, W. Chen, W. Zheng, X. Jiang, K. Chen, C. Qi, D. Ma, Gd-doped CuBi2O4/CuO heterojunction film photocathodes for photoelectrochemical H2O2 production through oxygen reduction. Nano Res.,2021, 14, 3439–3445. https://doi.org/10.1007/s12274-021-3638-y.